NJC

ROYAL SOCIETY OF CHEMISTRY

PAPER

View Article Online
View Journal | View Issue

Cite this: *New J. Chem.*, 2026, **50**, 3794

Climate-adaptive photothermal superhydrophobic CA/PU membrane for oil–water separation

Enyu Wei,† Ye Zhang,† Linfei Pan and Lili Li *

Received 4th January 2026,
Accepted 4th February 2026

DOI: 10.1039/d6nj00024j

rsc.li/njc

Within the realm of membrane separation technology, low temperatures can lead to an increase in oil viscosity and the freezing of water, resulting in a significant decline in separation efficiency. Herein, a climate-adaptive photothermal superhydrophobic membrane (CA/PU_3-PZ) was prepared through layer-by-layer assembly of polydopamine (PDA) coating and hydrophobic-modified ZIF-8 (ZIF-8-M) particles onto a cellulose acetate/polyurethane (CA/PU) electrospun membrane. The incorporation of PU into the CA matrix enhanced the tensile strength of the membrane from 0.14 MPa to 1 MPa. The CA/PU_3-PZ demonstrated exceptional oil–water separation performance. Notably, its separation capability can be fully restored to the original level within 10 minutes under light exposure, even after freezing at low temperatures. Furthermore, the CA/PU_3-PZ membrane exhibited outstanding anti-icing capability, with the freezing duration of droplets on its surface significantly prolonged to 981 s. This presented a streamlined, economically viable, and eco-friendly method for fabricating oil–water separation membrane materials that exhibited temperature adaptability.

1. Introduction

In recent decades, the ever-increasing scale of human industrial and domestic activities has driven substantial generation of oily wastewater across sectors, such as petroleum extraction, textile manufacturing, chemical synthesis, and food service industries.[1–4] This category of wastewater poses significant ecological hazards to aquatic ecosystems. In traditional membrane separation methods, membrane separation technology has the most extensive application due to its advantages of simple operation, high separation efficiency and low energy consumption.[5–9] For superhydrophobic membranes, surface modification is typically carried out using low-surface-energy fluorinated compounds.[10] Nevertheless, these materials pose a range of toxicological risks.[11–15] The development of fluorine-free hydrophobic materials emerges as an imperative and highly significant issue.

The membrane technology employed for oil–water separation faces several crucial challenges, including performance issues at low temperatures and potential environmental hazards.[16–18] In low-temperature environments, the rise in oil-phase viscosity can significantly diminish the effectiveness in oil–water separation. Moreover, the water phase may freeze within the membrane, further exacerbating the issue.[19,20] Owing to the interlocking mechanism, the ice on the membrane surface exhibits enhanced adhesion strength, making its removal a challenging task.[21] In comparison, conventional de-icing methods may damage the micro-nano structure of the separation membrane, consequently resulting in a deterioration of its separation performance.[22–24] Therefore, to improve the stability of membrane materials in low-temperature environments and expand their application scope under such conditions, it is of paramount urgency to develop an oil–water separation membrane with climate adaptability.

Furthermore, the high production costs and potential environmental hazards have hindered its large-scale application. Currently, researchers are directing increasing attention towards environmentally-friendly materials.[25] Cellulose acetate (CA), a biomass-based material produced *via* the deacetylation of cellulose, boasts numerous remarkable advantages, encompassing non-toxicity, excellent film-forming property, low cost, and good biocompatibility.[26,27] However, in the course of the actual oil–water separation process, the mechanical properties of CA fall short of expectations.[25] Moreover, due to its inherent hydrophilicity, CA is prone to swelling in water. The modification of CA by combining it with other polymer chains has been demonstrated to be an efficient strategy.[28,29]

In this study, a fluorine-free CA-based oil–water separation membrane was fabricated through the integration of electrospinning and layer-by-layer self-assembly methods. During the electrospinning process, the insertion of PU molecular chains into the CA structure enhanced its mechanical properties. Fluorine-free, low-toxicity, and biodegradable oleic acid was

Key Laboratory of Automobile Materials, Ministry of Education, and College of Materials Science and Engineering, Jilin University, Changchun 130022, China. E-mail: lilyllee@jlu.edu.cn

† These two authors are joint first authors.

utilized as the modifying agent to synthesize hydrophobic ZIF-8-M particles. The loading of PDA and ZIF-8-M endowed the membrane material with excellent photothermal conversion performance and hydrophobicity, respectively. Scanning electron microscopy (SEM), X-ray diffraction (XRD), energy-dispersive X-ray spectroscopy (EDS) and X-ray photoelectron spectroscopy (XPS) were utilized to investigate the microscopic structure and chemical composition of the membrane. Furthermore, a comprehensive set of tests was carried out to assess various properties of the membrane, including its wettability, oil–water separation capacity, photothermal characteristics, anti-icing property, and photothermal de-icing performance.

2. Experimental

2.1. Materials

Zinc nitrate ($Zn(NO_3)_2$), tetrachloromethane (CCl_4), petroleum ether, Sudan III, NaCl, NaOH, HCl, methanol and ethanol were procured from Beijing Chemical Plant. Dopamine hydrochloride (DA, 98%, AR), copper(II) sulfate pentahydrate ($CuSO_4{\cdot}5H_2O$, AR), hydrogen peroxide (H_2O_2) (30%, AR), 2-methylimidazole (2-MI), oleic acid, Span 80, *n*-hexane, *n*-heptane methylene blue (MB), malachite green (MG), cellulose acetate (CA, with an acetyl content of 39.8% and a hydroxyl content of 3.5%), tris(hydroxymethyl)-aminomethane (Tris), *N*,*N*-dimethylformamide (DMF) and tetrahydrofuran (THF) were supplied by Shanghai Macklin Biochemical Technology. The polyurethane (PU) was synthesized in accordance with the previous research conducted by our group.[30] Deionized water (DI water) was obtained from the laboratory's water-purifying system.

2.2. Preparation of CA/PU_3-PZ composite membrane

2.2.1. Preparation of Hydrophobically modified ZIF-8 (ZIF-8-M). A quantity of 2.5 g of $Zn(NO_3)_2$ and 1.5 g of 2-MI were dissolved in 50 mL of methanol. Subsequently, 6 mL of oleic acid was introduced into the solution, and the mixture was stirred uniformly at a rotational speed of 250 rpm. After a reaction period of 24 hours, the mixed solution underwent centrifugation at a speed of 8500 rpm for 10 minutes to isolate the particles. The obtained particles were then subjected to multiple rinsing cycles, alternating between ethanol and DI water. Finally, the rinsed particles were dried under vacuum at a temperature of 50 °C. The particles were designated as ZIF-8-M.

2.2.2. Preparation of CA/PU_3-PZ membrane

CA/PU_x membranes. The preparation of CA/PU_x membranes was presented in Note S1. Based on the performance tests, CA/PU_3 membrane was selected as the substrate membrane.

CA/PU_3-P membrane. The DA-containing Tris buffer was prepared by sequentially dissolving 50 mM Tris, 200 mg DA, 5 mM $CuSO_4{\cdot}5H_2O$, and 19.6 mM H_2O_2 in 100 mL DI water. Subsequently, the CA/PU_3 membrane was soaked in the DA-containing Tris buffer for 4 h to prepare the CA/PU_3-P membrane.

CA/PU_3-PZ membrane. A quantity of 1 g of ZIF-8-M was dispersed in 100 mL of ethanol through ultrasonication. The CA/PU_3-P membrane was immersed in the ZIF-8-M ethanol dispersion and ultrasonicated for 6 h. Subsequently, the membrane was rinsed with water and ethanol to obtain CA/PU_3-PZ membrane. Fig. 1 illustrated the detailed process for preparing CA/PU_3-PZ membrane.

2.3. Characterizations

The characterizations employed in this study could be found in Note S2 of the SI.

2.4. The oil–water separation and reusability

The CA/PU_3-PZ membrane, possessing an effective penetration area of 19.6 cm^2, was positioned within a glass filtration device. The upper funnel was filled with a mixture consisting of 50 mL of oil (*n*-hexane, tetrachloromethane, petroleum ether, or *n*-heptane) and 50 mL of water. The tests were carried out exclusively under the driving force of gravity. The measurements of reusability were acquired by repeating the above steps. The oil

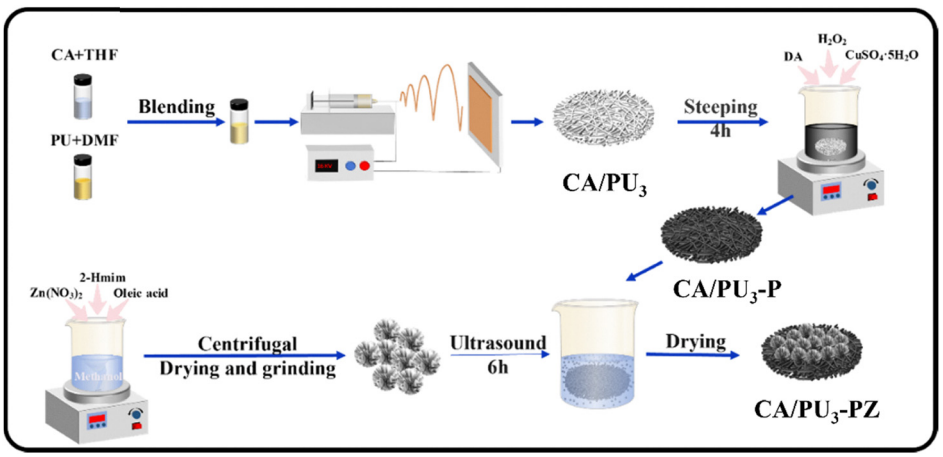

Fig. 1 The preparation of CA/PU_3-PZ membrane.

flux was determined through calculating using eqn (1):[31]

$$\text{Flux} = \frac{V}{St} \quad (1)$$

The variable V signifies the volume of the oil (L). The area of the separation membrane is denoted by S, with the unit of square meters (m^2), while t represents the separation time, measured in hours (h). The separation efficiency (φ_1) could be calculated according to eqn (2):[30]

$$\varphi_1 = \frac{V_1}{V_0} \quad (2)$$

The variable V_0 and V_1 are employed to represent the oil volumes before and after separation, respectively.

For the preparation of the surfactant-stabilized water-in-oil emulsion, 0.1 g of Span 80 was dissolved in 99 mL oil (*n*-hexane, tetrachloromethane, petroleum ether, or *n*-heptane),followed by the addition of 1 mL DI water. To create a stable emulsion, the mixture was subjected to vigorous swirling for a duration of 6 h. Eqn (1) was utilized to determine the separation flux. Karl Fischer moisture titrator was used to measure the water content in order to assess the separation efficiency (φ_2). Eqn (3) is presented below:[32]

$$\varphi_2 = \left(1 - \frac{C_1}{C_0}\right) \times 100\% \quad (3)$$

where C_0 and C_1 are utilized to denote water content (ppm) before and after separation, respectively. The measurements of reusability were obtained by repeating the aforementioned steps.

2.5. Oil adsorption tests

The CA/PU_3-PZ membrane was immersed in a glass dish with CCl_4. The adsorption capacity of the membrane was characterized under dark and light conditions. The oil adsorption capacities (q) were determined by using eqn (4):[33]

$$q = \frac{m_f - m_0}{m_0} \quad (4)$$

where m_f and m_0 represents the weight (g) of the membrane after and before oil adsorption, respectively.

2.6. Anti-icing test and photothermal de-icing test

Anti-icing test. The samples were positioned on a semiconductor cooling plate, and the temperature was precisely controlled at −10 °C to simulate a cold environment. A 100-μL DI water droplet was added to the sample surface. The temporal changes in the morphology of the droplet on the membrane surface were captured using a high-speed camera. Complete droplet opacity indicates full freezing. The freezing time was measured as the liquid–solid transition interval.

Photothermal de-icing test. The samples were positioned on a semiconductor cooler, and the temperature was precisely adjusted to −10 °C. Subsequently, a 0.5-mL ice layer was formed on the surface of samples. After that, the ice was subjected to simulated irradiation with an intensity of 1 sun (1000 W m^{-2}), and the entire melting process was recorded in detail.

2.7. Stability testing

Chemical stability evaluation: To assess the chemical stability of CA/PU_3-PZ, the samples were separately immersed in solutions with a range of pH values (1, 3, 5, 7, 9, 11, and 13) and 10 wt% NaCl solution for 8 hours. Subsequently, the samples were taken out, rinsed with deionized water, and then dried. The water contact angle (WCA) and oil–water separation capabilities of the CA/PU_3-PZ membranes were evaluated.

Mechanical durability tests: The mechanical durability of the superhydrophobic surface on the CA/PU_3-PZ membranes were examined through two distinct methods: abrasion testing using a 100 g weight and adhesion testing with adhesive tape. Subsequently, the WCAs were measured.

3. Result and discussion

3.1. Morphology of CA/PU_3-PZ membrane

The SEM images of the CA/PU_x membranes were presented in Fig. S1 and S2. Based on the evaluations of mechanical properties and water flux, the CA/PU_3 membrane was selected for subsequent surface functionalization (Fig. S3 and S4). The CA/PU_3 membrane was composed of smooth and continuous fibers (Fig. 2a). After the loading of PDA, the membrane surface became densely populated with a substantial quantity of particles (Fig. 2b and c).[34] Following the loading of ZIF-8-M particles, the membrane surface was covered with a large number of particles (Fig. 2d and e). The EDS results revealed that the C, N and O elements were uniformly distributed in CA/PU_3-PZ, while Zn elements were concentratedly distributed on the particles (Fig. 2f–i and Fig. S5). Fig. S6 illustrated the surface roughness characteristics of the CA/PU-based membranes. The arithmetic mean roughness (R_a) value of CA/PU_3 membrane was 2.811 ± 0.681 μm (Fig. S6a). After PDA coating, the R_a value of the fiber membrane surface increased to 8.398 ± 0.939 μm (Fig. S6b). Following the loading of ZIF-8-M particles, the CA/PU_3-PZ membrane exhibited the highest R_a value of 12.896 ± 1.694 μm (Fig. S6c). All these results confirmed that the loading of PDA and ZIF-8-M particles led to an elevation in the surface roughness of the membrane.

3.2. Components analysis

The FTIR spectra of the CA/PU-based membranes were depicted in Fig. 3a. Within the FTIR spectrum of the CA/PU_3 membrane, the 3488 cm^{-1} (O–H stretching) and 1034 cm^{-1} (C–O stretching) bands corresponded to CA, while the PU component exhibited the characteristic peaks at 3329 cm^{-1} (N–H stretching vibration), 1597 cm^{-1} (aromatic C=C stretching vibration), and 1527 cm^{-1} (N–H bending vibrations) (Fig. S7).[35,36] Compared with the CA/PU_3 membrane, the CA/PU_3-P membrane exhibited a broadened absorption peak at 3325 cm^{-1}, which was attributed to overlapping O–H and N–H stretching vibrations. This spectral feature indicated the loading of PDA.[37] After the

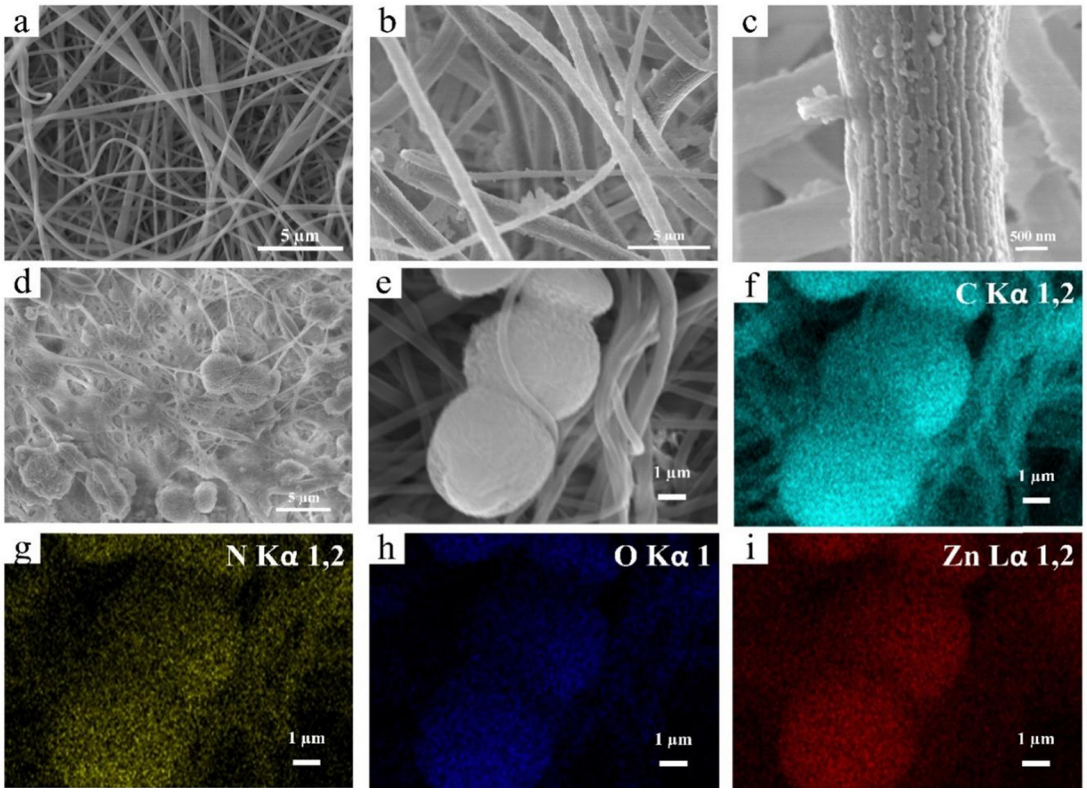

Fig. 2 The morphology of (a) CA/PU_3, (b) and (c) CA/PU_3-P and (d) and (e) CA/PU_3-PZ membranes; EDS results of CA/PU_3-PZ membrane: mapping images with (f) C (greenish), (g) N (yellow), (h) O (blue) and (i) Zn (red).

loading of ZIF-8-M particles, the characteristic peak of the –OH group disappeared, which was ascribed to the formation of coordination between the –OH of PDA and ZIF-8-M.[38] In addition, the characteristic peak at 736 cm^{-1} corresponded to the out-of-plane bending vibration of C–H bonds in ZIF-8-M, providing evidence for the successful loading of ZIF-8-M particles (Fig. S8).

Fig. 3b presented the XPS spectra of the CA/PU-based membranes. Compared to the CA/PU_3 membrane, the XPS spectrum of CA/PU_3-P membrane exhibited a distinct N 1s peak at 400.0 eV, which served as confirmation of the presence of a PDA coating layer (Fig. S9). The XPS survey spectra of the CA/PU_3-PZ membrane exhibited distinct Zn 2p peaks at 1044.9 eV (Zn $2p_{1/2}$) and 1021.8 eV (Zn $2p_{3/2}$), which confirmed the loading of ZIF-8-M particles. As shown in Fig. 3c–e, the high-resolution C 1s spectrum of CA/PU_3, CA/PU_3-P, and CA/PU_3-PZ membranes displayed five distinct peaks at 284.8 eV (C–C/C–H/C═C), 285.3 eV (C–N), 286.6 eV (C–O), 288.7 eV (C═O), and 289.3 eV (–NH–COO–).[39] Compared with CA/PU_3 membrane, the CA/PU_3-P membrane exhibited an elevation in the proportions of C–N and C–O bonds, concurrent with a reduction in the proportion of C–C/C–H/C═C bonds, which indicated the loading of PDA on the membrane surface. After the loading of ZIF-8-M particles, the proportion of C–H/C–C/C═C bond of the CA/PU_3-PZ membrane increased significantly, whereas the proportions of other characteristic peaks decreased. In Fig. 3f, the peak at 531.5 eV of the CA/PU_3-PZ membrane was assigned to Zn–O coordination, which originated from the ZIF-8-M particles (Fig. S10b). Besides, the high-resolution XPS spectra of Zn 2p for the CA/PU_3-PZ membrane could be precisely deconvoluted into two separate peaks, which were located at 1044.9 eV (Zn $2p_{1/2}$) and 1021.8 eV (Zn $2p_{3/2}$) (Fig. 3g). The results provided solid evidence for the loading of ZIF-8-M particles onto the CA/PU_3-P membrane. Collectively, these results offered substantial evidence supporting the deposition of ZIF-8-M particles on the surface of the CA/PU_3-P membrane.

3.3. Wettability and mechanical properties analysis

Fig. 3h presented the tensile tests of the CA/PU-based membranes. The CA/PU_3 membrane demonstrated a tensile strength of 1.01 MPa and an elongation at break of 4.9%.The tensile strength of CA/PU_3 membrane was markedly higher than that of CA nanofiber membranes (0.19 MPa) (Fig. S4a) In contrast, the CA/PU_3-P membrane achieved a tensile strength of 3.58 MPa and a fracture elongation of 15.08%. This enhancement was presumably attributed to the hydrogen-bonding interactions among fibers after the loading of PDA, thereby reinforcing the mechanical strength of the membrane.[40,41] Compared with the CA/PU_3-P membrane, the tensile strength of the CA/PU_3-PZ membrane decreased to 2.12 MPa, and its elongation at break dropped to 2.89%. This could potentially be attributed to the partial shedding of PDA from the membrane surface during ultrasonic treatment. Nevertheless, the mechanical properties of CA/PU_3-PZ membrane still met the usage requirements.

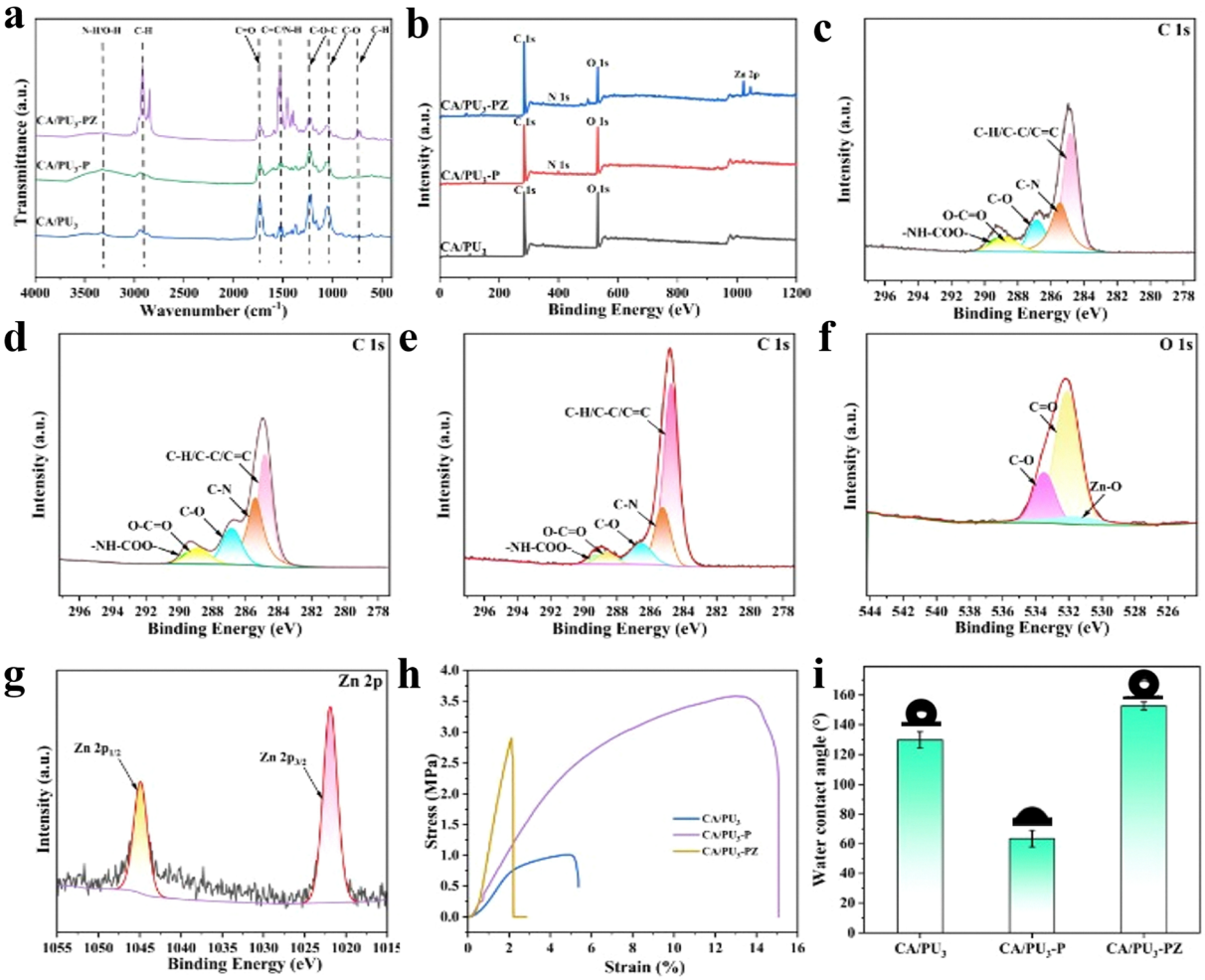

Fig. 3 (a) FTIR spectrum of CA/PU-based membranes; (b) XPS survey spectra of CA/PU-based membranes; High-resolution C 1 s spectrum of (c) CA/PU_3, (d) CA/PU_3-P, and (e) CA/PU_3-PZ membranes. High-resolution (f) O 1 s, and (g) Zn 2p spectrum of CA/PU_3-PZ membrane; (h) tensile tests of CA/PU-based membranes; (i) WCAs of CA/PU-based membranes.

Fig. 3i showed the WCAs of the CA/PU-based membranes. The CA/PU_3 membrane exhibited a WCA of 129.8°. The WCA of the CA/PU_3-P membrane dropped to 63.4°, and it was wetted completely within 0.3 seconds (Fig. S11), which primarily resulted from the numerous hydrophilic groups of PDA on the surface.[42] After loading with ZIF-8-M, the WCA of the CA/PU_3-PZ membrane exhibited an increase, rising from 63.4° to 152.6°.

3.4. The oil–water separation performance of CA/PU_3-PZ composite membrane

The schematic diagram of the experimental setup for oil–water separation was presented in Fig. S12. The fluxes of the CA/PU_3-PZ membrane for *n*-hexane, tetrachloromethane, petroleum ether, and *n*-heptane were measured as 1584.39, 2253.18, 2006.37, and 2257.16 L m^{-2} h^{-1}, respectively (Fig. 4a). The CA/PU_3-PZ membrane demonstrated separation efficiencies surpassing 99.60% for all the tested oil–water mixtures. The variation in flux among these oil–water mixtures could be attributed to differences in oil viscosity.[43] To assess durability of the CA/PU_3-PZ membrane, a 10-cycle separation test was conducted with an *n*-hexane–water mixture. As depicted in Fig. 4b, after 10 cycles, the membrane maintained a flux of 1415.12 L m^{-2} h^{-1} and a separation efficiency of 98.8%, thereby demonstrating its outstanding reusability. Fig. 4c and d were the water-in-oil emulsion separation experiments. Initially, the emulsion presented an opaque white coloration (Fig. S13a). The emulsion droplets with an average diameter of 222.7 ± 44.31 nm were uniformly distributed (Fig. S13c). After separation using the CA/PU_3-PZ membrane, the emulsion turned clear (Fig. S13b). The average diameter of the emulsion droplets underwent a significant reduction, which dropped to 11.17 ± 1.537 nm (Fig. S13d). For *n*-hexane, tetrachloromethane, petroleum ether and *n*-heptane, the emulsion separation fluxes were 665.38, 788.22, 585.19, and 597.14 L m^{-2} h^{-1}, respectively, while the corresponding separation efficiencies were 98.6%, 98.9%, 98.3%, and 98.5% (Fig. 4c). Fig. 4g demonstrated the reusability of the CA/PU_3-PZ membrane. Following 10 consecutive separation cycles, the CA/PU_3-PZ membrane maintained an emulsion separation efficiency exceeding 97.0% and a flux rate

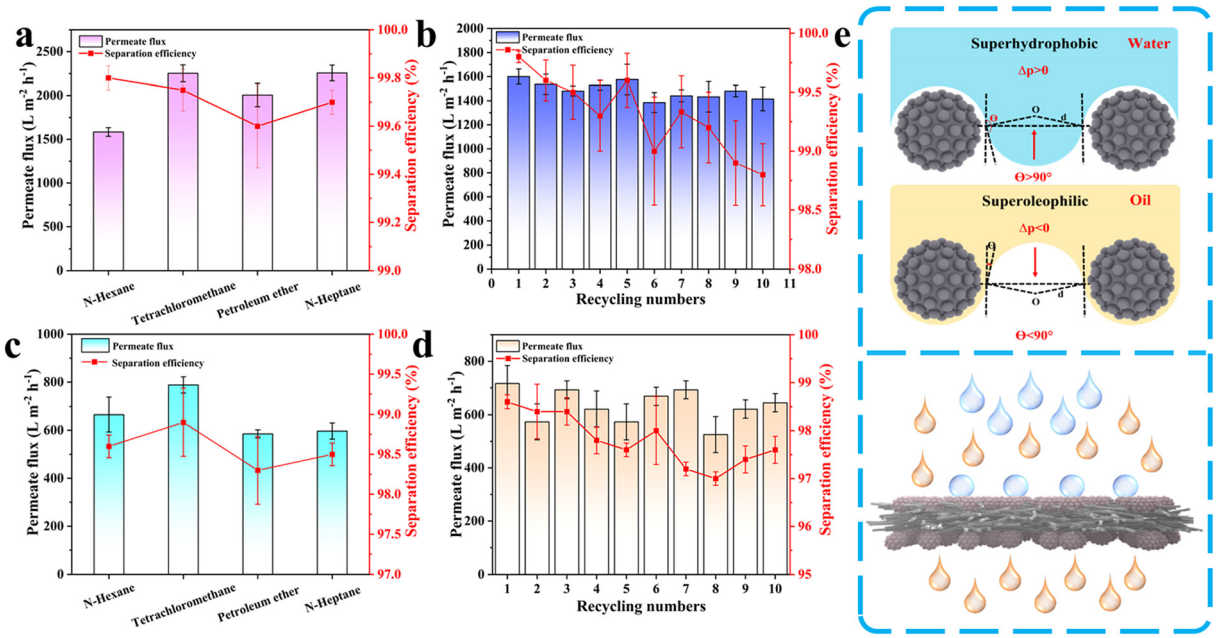

Fig. 4 (a) Separation flux and efficiency of CA/PU_3-PZ membrane for oil–water mixtures; (b) recycling performance of CA/PU_3-PZ membrane for *n*-hexane–water mixtures; (c) separation flux and efficiency of CA/PU_3-PZ membrane for oil–water emulsions; (d) recycling performance of CA/PU_3-PZ membrane for water-in-*n*-hexane emulsions; (e) the principle for gravity separation of oil–water mixtures.

above 573.25 L m^{-2} h^{-1} (Fig. 4d). These findings indicated that the CA/PU_3-PZ membrane had long-term reusability in practical applications.

The possible separation mechanism was presented in Fig. 4e. The intrusion pressure (Δp), defined as the minimum pressure necessary for the liquid to wet the membrane pores, could be characterized by the Young–Laplace equation:[44]

$$\Delta p = -\frac{2\gamma\cos(\theta)}{d} \quad (5)$$

where θ denotes the liquid contact angle, γ represents the surface tension between oil and water, and d signifies the size of the interfiber pores. Therefore, the key factors that exerted influence on the efficiency of membrane separation are its effective pore size and wetting properties. After ZIF-8-M particles loading, the membrane showed maximum surface roughness (12.896 ± 1.694 μm) and superhydrophobicity. As illustrated in Fig. 4e, when a water droplet impacted the surface of the CA/PU_3-PZ membrane, the membrane generated an upward force on the water droplet, effectively preventing water from permeating. Conversely, when oil contacted the CA/PU_3-PZ membrane, the oil droplet experienced a downward attractive force which led to the rapid penetration through the membrane structure. Moreover, the air pockets trapped at the interface of particle-water droplet might impede water droplet wetting. Consequently, the CA/PU_3-PZ membrane demonstrated an exceptionally high separation performance in the separation of oil–water mixtures.

3.5. Photothermal-driven performance recovery of separation membranes at low temperature

When exposed to sub-zero temperature, the membrane surface exhibited ice adhesion *via* mechanical interlocking at the coating-ice interface.[45,46] This architecture markedly augmented the adhesive force between the ice and the membrane surface, consequently the process of ice removal was difficult. Moreover, during the long-term low-temperature oil–water separation experiments, it was observed that the performance of the separation membrane significantly declined due to ice crystals (Fig. 5d). Owing to the abundance of benzene rings in PDA, it exhibited strong π–π conjugation and exceptional absorption of visible to near-infrared (NIR) light.[47–50] Consequently, the CA/PU_3-PZ membrane was anticipated to leverage the photothermal conversion properties of PDA for non-destructive photothermal de-icing. In Fig. 5a–c, the photothermal conversion performance of the CA/PU-based membranes was investigated. In Fig. 5a, the UV-vis spectra demonstrated that the CA/PU_3 membrane exhibited poor absorption capacity for visible light. After PDA coating, the CA/PU_3-P membrane exhibited significantly enhanced visible light absorption. However, the visible light absorption capacity of the CA/PU_3-PZ membrane after loading with ZIF-8-M showed a slight decrease. Combined with XPS analysis, this phenomenon might be attributed to the fact that the surface ZIF-8-M coating affected the light absorption of PDA. Fig. 5b and c illustrated the trend of the surface temperature of the membrane with increasing irradiation time. The surface temperature of the CA/PU_3 membrane increased 5.5 °C after a 10-minute irradiation by simulated sunlight. For the CA/PU_3-P membrane and the

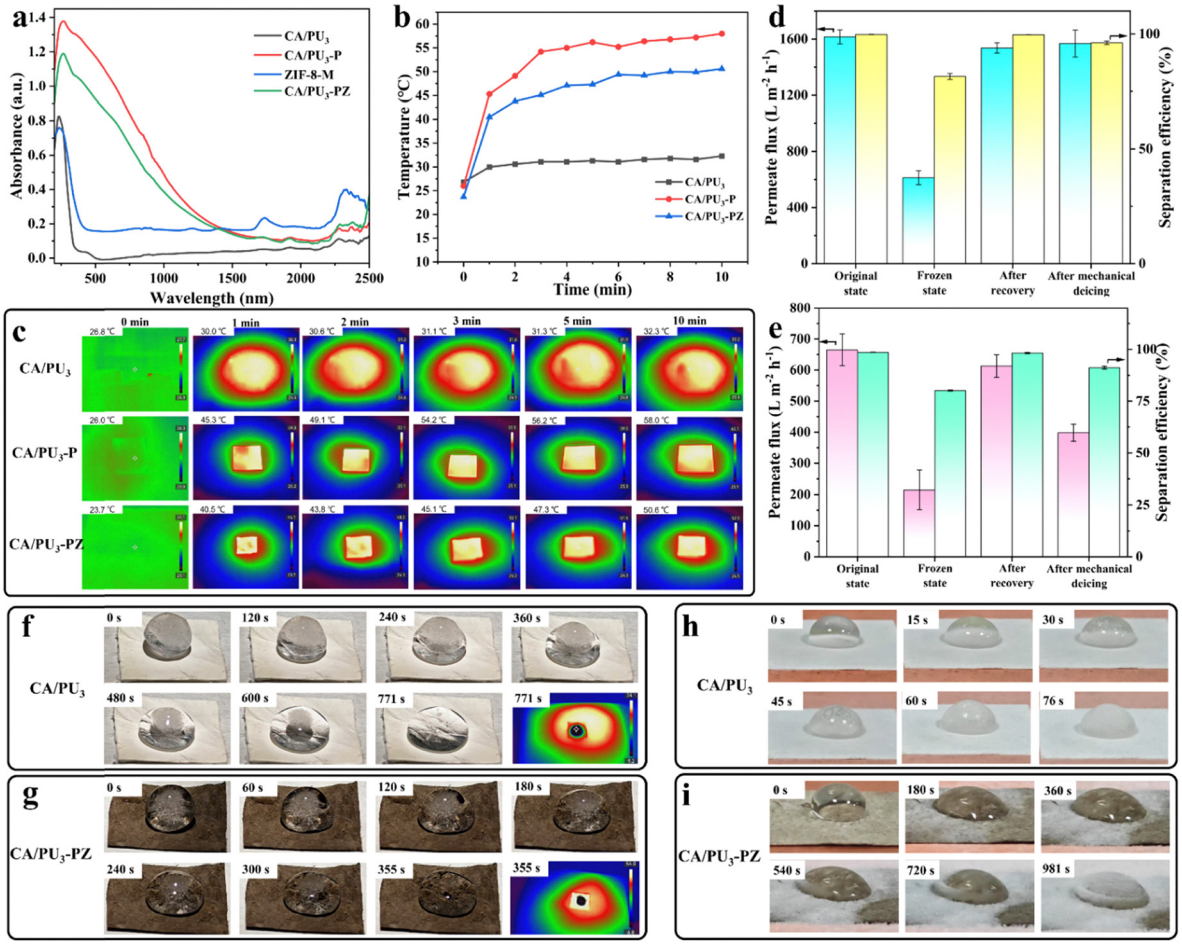

Fig. 5 (a) UV-vis spectrum of CA/PU-based membranes and ZIF-8-M particles. (b) Changes in surface temperature of CA/PU-based membranes. (c) Temperature variations on the membrane surface during a 10-minute exposure under 1-sun illumination for CA/PU-based membranes. The membrane separation performance of CA/PU_3-PZ membrane for (d) oil–water mixture and (e) water-in-oil emulsion after being in frozen state, light recovery and mechanical defrosting. Optical images of photothermal de-icing process and the corresponding optical thermal images upon complete ice melting on (f) CA/PU_3 and (g) CA/PU_3-PZ membranes. Optical images of freezing process of water droplets on (h) CA/PU_3 and (i) CA/PU_3-PZ membranes.

CA/PU_3-PZ membrane, within five minutes, their surface temperatures rose to 56.2 °C and 47.3 °C, respectively. The surface temperature evolution of membranes correlated precisely with the absorbance modifications. As shown in Fig. 5a, ZIF-8-M exhibited strong absorption capacity for ultraviolet light but relatively weak absorption for visible and NIR light, leading to limited photothermal conversion capability. After loading ZIF-8-M onto the surface of CA/PU_3-P membrane, the absorption of the membrane in NIR and visible light decreased. Consequently, the photothermal conversion performance of the CA/PU_3-PZ membrane declined.

The simulated de-icing experiments were conducted under 1-sun solar irradiation at an ambient temperature of −10 °C. Specifically, ice crystals were uniformly deposited on the composite membrane surface, and the melting state of the ice crystals over time was recorded followed by light irradiation. For the CA/PU_3 membrane, the ice crystal on its surface underwent complete melting within 771 s (Fig. 5f). In comparison, the ice crystal on the surface of CA/PU_3-PZ membrane achieved full melting within 355 s, representing a 54.0% decrease in melting time (Fig. 5g). The de-icing performance depended not only on its photothermal effect but also on its water-binding capacity. The CA/PU_3-P exhibited excellent photothermal conversion efficiency but is also highly hydrophilic (Fig. 3i). After multiple photothermal de-icing cycles, its hydrophilic nature caused water to penetrate the membrane, thereby enhancing the adhesion between ice and CA/PU_3-P membrane. Consequently, the freezing time of ice was shortened, and the photothermal de-icing time was prolonged (Fig. S14).The results demonstrated that the CA/PU_3-PZ membrane exhibited exceptional photothermal de-icing performance. Based on the photothermal de-icing property of the CA/PU_3-PZ membrane, the oil–water separation performance during low-temperature icing and after photothermal de-icing was evaluated (Fig. 5c). In oil–water mixture separation tests, after ice formation on the membrane surface, the separation flux dropped to 613.06 L m^{-2} h^{-1} and the separation efficiency decreased to 81.5%. Following photothermal irradiation, the flux and separation

efficiency of CA/PU_3-PZ membrane recovered to 1536.62 L m^{-2} h^{-1} and 99.7%, respectively. Similar phenomena were observed in water-in-oil emulsion separation tests. Post-freezing, the flux and separation efficiency of CA/PU_3-PZ membrane decreased to 214.97 L m^{-2} h^{-1} and 81.3%, then they were restored to 613.05 L m^{-2} h^{-1} for the flux and 98.27% for separation efficiency after photothermal treatment. This fully demonstrated that the oil–water separation performance was effectively restored that was impaired by freezing. In comparison, after using mechanical de-icing, the WCA of the CA/PU_3-PZ decreased to 135.2° (Fig. S15). Compared with the initial membrane, the separation fluxes of the membrane for both oil–water mixtures and water-in-oil emulsions could be restored to the levels prior to icing. This is because the separation flux was mainly influenced by pore sizes of the separation membrane. However, its separation efficiency decreased significantly. This was probably because mechanical de-icing damaged the micro-nanoscale structures of CA/PU_3-PZ, thereby affecting its hydrophobicity and separation efficiency. These results further demonstrate that the membrane possesses non-destructive de-icing characteristics through photothermal driving.

3.6. Anti-icing performance

In addition to photothermal de-icing capabilities, the anti-icing performance of the separation membrane also served as a crucial metric for evaluating its functionality under cold conditions.[51,52] For cotton, copper, and stainless steel, the surface freezing times were 79.3 s, 95 s, and 7.3 s, respectively.[53–55] The inherent anti-icing property of the membranes was evaluated (Fig. 5f–j). The freezing duration of water droplets on the CA/PU_3 membrane was 76 s (Fig. 5f). In contrast, the freezing time of water droplets on the CA/PU_3-PZ membrane was substantially prolonged to 981 s, which was substantially higher than that of CA/PU_3 membrane as well as other reported substrate materials (Fig. 5j). The CA/PU_3-PZ membrane demonstrated exceptional anti-icing performance, which primarily stemmed from its hierarchical micro-nano structures. These micro-nano structures, capable of trapping air, could form a stable thermal insulation layer, thus reducing the efficiency of heat conduction between supercooled droplets and the substrate.[56] Additionally, the superhydrophobicity of membrane minimized the contact area of droplet-substrate, thereby effectively delaying droplet freezing. Compared with other reported literatures, the CA/PU_3-PZ membrane exhibited high separation efficiency, the shorter photothermal de-icing time and the longer delayed freezing duration (Table S1).[57–63]

3.7. The stability of CA/PU_3-PZ membrane

Fig. 6 showed the stability test results of the CA/PU_3-PZ membrane. Fig. 6a and b specifically depicted the oil–water separation performance and WCA of the CA/PU_3-PZ membrane following immersion in solutions with varying pH values and high salinity environments (simulated seawater). The membrane maintained stable oil–water separation performance in the

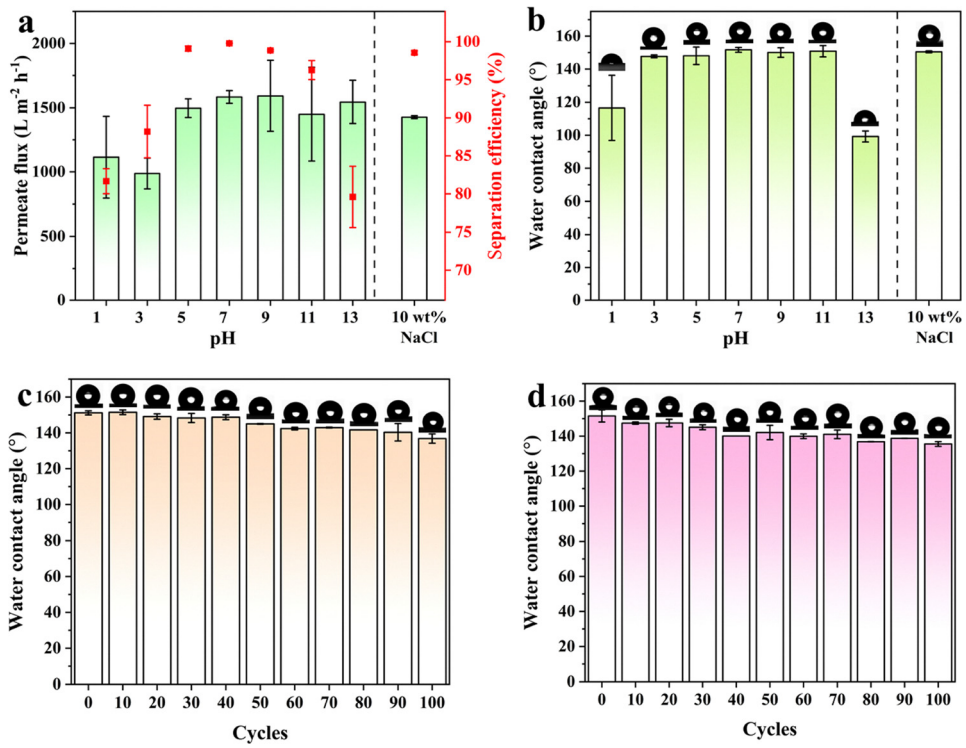

Fig. 6 Chemical and mechanical stability evaluation of CA/PU_3-PZ membrane. Chemical stability under different pH and high-salt solutions: (a) oil–water separation performance and (b) WCA. Mechanical stability: (c) abrasion with a 100 g weight and (d) scratching with adhesive tape.

pH range from 5 to 11. However, when the pH is less than 5 or greater than 11, the oil–water separation efficiency of CA/PU_3-PZ membrane decreased (Fig. 6a). Meanwhile, the WCA also exhibited similar changes. The alteration in wettability led to variations in separation efficiency. Additionally, in the simulated seawater environment with high salinity, the membrane exhibited a slight reduction in oil–water separation capability and WCA. The separation flux, efficiency and WCA decreased to 1426.75 L m^{-2} h^{-1}, 98.57% and 150.47°. The results demonstrated that the CA/PU_3-PZ membrane exhibited stable performance in high-salt environments.

Fig. 6c and d illustrated the mechanical stability tests results of the CA/PU_3-PZ membrane. After cyclic abrasion with a 100 g weight for 30 cycles, the WCA remained at 148.3 ± 2.55°. Following 20 adhesive tape peeling cycles, the WCA decreased to 147.5 ± 2.12°. These all proved that the CA/PU_3-PZ membrane exhibited good mechanical stability.

4. Conclusion

In this study, a photothermal superhydrophobic CA/PU_3-PZ composite membrane was successfully fabricated. The integration of PU and the incorporation of PDA particles substantially enhanced the tensile properties of the membrane. Moreover, the introduction of PDA endowed the membrane with favorable photothermal performance, and the addition of ZIF-8-M particles conferred hydrophobic properties upon the membrane.The superhydrophobicity endowed the CA/PU_3-PZ membrane with outstanding oil–water separation performance. The CA/PU_3-PZ membrane demonstrated a flux of 1584.39 L m^{-2} h^{-1} and a separation efficiency of 99.60% for oil–water mixtures. For oil–water emulsions, it exhibited a flux of 665.38 L m^{-2} h^{-1} and a separation efficiency of 98.6%. Furthermore, the CA/PU_3-PZ membrane exhibited photothermal performance, with its surface temperature rising to 47.3 °C within five minutes. Based on the membrane's photothermal conversion ability, the CA/PU_3-PZ membrane was capable of achieving non-destructive de-icing and restoring its oil–water separation performance. In the separation of oil–water mixtures, the membrane's flux rebounded from 613.06 L m^{-2} h^{-1} to 1536.62 L m^{-2} h^{-1}, and the separation efficiency recovered from 81.5% to 99.7%. For the separation of water-in-oil emulsions, the membrane flux increased from 214.97 L m^{-2} h^{-1} to 613.05 L m^{-2} h^{-1},and the separation efficiency rose from 81.3% to 98.27%. In addition, it also demonstrated favourable anti-icing properties. Compared with the CA/PU_3 substrate membrane, the freezing time of droplets on the surface of the CA/PU_3-PZ membrane was significantly extended, from 76 s to 981 s. The preparation of this membrane was simple, cost-effective, fluorine-free, and environmentally friendly, meeting the requirements for oil–water separation in various environments.

Author contributions

Enyu Wei: writing – original draft, conceptualization, data curation, methodology. Ye Zhang: conceptualization, writing – review & editing, resources. Linfei Pan: conceptualization, software. Lili Li: methodology, resources, funding acquisition, writing – review & editing.

Conflicts of interest

There are no conflicts to declare.

Data availability

The authors declare that the data supporting the findings of this study are available within the paper and its supplementary information (SI) files. Supplementary information include the preparation of CA/PU membrane, characterizations, particle size distributions, the cyclic de-icing test of CA/PU_3-P membrane, tensile test, roughness images, *etc*. See DOI: https://doi.org/10.1039/d6nj00024j.

Acknowledgements

This research was supported by the General Project of Jilin Provincial Natural Science Foundation (20250102117JC).

References

1 X. Wang and X. Li, Stabilized superhydrophobic composite membranes prepared by electrospinning for oil–water separation, *Polym. Adv. Technol.*, 2024, **35**(3), e6329.
2 Y. Xu, J. Liao, R. He, S. Yang, Z. Luo, M. Xu, Y. Tao and X. Wang, Superhydrophobic and oleophilic polyurethane sponge for oil/water separation, *Mater. Today Commun.*, 2024, **38**, 107658.
3 P. Pi, Z. Ren, Y. Yang, W. Chen and Y. Lin, A review of various dimensional superwetting materials for oil–water separation, *Nanoscale*, 2024, **16**(37), 17248–17275.
4 T.-T. Li, M. Jia, S. Li, Y. Zhang, X. Wang, S. Chu, B.-C. Shiu, C.-W. Lou and J.-H. Lin, Solar-driven pH-responsive oil–water separation membranes for effective oil–water emulsion separation, *New J. Chem.*, 2024, **48**(21), 9549–9558.
5 W. Zhu, N. Tang, C. Jia and Y. Zhang, A superwetting rough structured nanofibrous membrane with enhancing antifouling performance for oil–water separation, *Sep. Purif. Technol.*, 2025, **359**, 130800.
6 J. Jiang, S. Wan, C. Wen, L. Tang and N. Xu, Frontiers in Innovative Materials and Technologies for Oil–Water Separation, *Polymers*, 2025, **17**(12), 1635.
7 Y. Xin, B. Qi, X. Wu, C. Yang and B. Li, Different types of membrane materials for oil-water separation: Status and challenges, *Colloid Interface Sci. Commun.*, 2024, **59**, 100772.
8 X. Hu, J. Li, S. Chen, C. Deng and G. Du, A self-cleaning Cu@MF–PG/GSH membrane for oil–water separation, *New J. Chem.*, 2025, **49**(43), 19035–19049.
9 B. Sun, X. Chen, Y. Jiang, L. Lin, D. Wang, R. Wang, C. Feng, G. Diao, Y. Piao, W. Zhang and H. Pang, Interface-Orchestrated Dual Microenvironments in CDMOF/MXene

for Selective Dye Adsorption and Lithium–Sulfur Battery Enhancement, *Adv. Funct. Mater.*, 2025, e26503.

10 W. Zhu, Y. Xing, H. Wang, M. Yu, H. Cen, L. Liu, Y. Li and W. Zhu, Fluorine-free preparation of superhydrophobic polyester fabric with directional moisture transport for efficient oil-water separation, *Colloids Surf., A*, 2024, **696**, 134369.

11 M. Scheringer, Innovate beyond PFAS, *Science*, 2023, **381**(6655), 251.

12 Z. Guo, M. Wang, L. Qiao and Z. He, Non-fluorinated lignin-based melamine sponges with superhydrophobic and photothermal properties for multi-functional applications, *Int. J. Biol. Macromol.*, 2024, **279**, 135168.

13 M. Wang, Z. Zhou, L. Qiao and Z. He, Constructing fluorine-free and photothermal MXene/candle soots-based superhydrophobic sponge for oil/water separation, crude oil recovery, and anti-icing, *Process Saf. Environ. Prot.*, 2025, **202**, 107738.

14 B. Long, B. Sun, L. Lin, Y. Jiang, Z. Yang, G. Diao, D. Feng, Y. Piao and W. Zhang, Radial wettability gradient core-shell fiber design enables synergistic solar reflection and moisture-driven cooling, *Chem. Eng. J.*, 2026, **527**, 171903.

15 B. Sun, D. Wang, Y. Jiang, R. Wang, L. Lyu, G. Diao, W. Zhang and H. Pang, Cyclodextrin Metal–Organic Framework Functionalized Carbon Materials with Optimized Interface Electronics and Selective Supramolecular Channels for High-Performance Lithium–Sulfur Batteries, *Adv. Mater.*, 2024, **36**(52), 2415633.

16 Z. Su, Y. Gao, J. Li, L. Wang, X. Yang, Y. Gao, X. Zhang and W. Lü, Superhydrophobic Coating with a Modified Micronano-ZnO@CoZIF-8 Structure for Efficient Anti-icing, *Langmuir*, 2025, **41**(37), 25684–25694.

17 J. Peng, X. Wang, J. Zhou, J. Wang, Y. Yang and Y. Mei, Photothermal/electrothermal superhydrophobic composite coating for efficient anti-icing and de-icing, *Composites, Part B*, 2026, **310**, 113144.

18 S. Yang, Q. Li, B. Du, Y. Ying, Y. Zeng, Y. Jin, X. Qin, S. Gao, S. Wang, Z. Wang, R. Wen and X. Ma, Photothermal superhydrophobic copper nanowire assemblies: fabrication and deicing/defrosting applications, *Int. J. Extreme Manuf.*, 2023, **5**(4), 045501.

19 Z. Xie, H. Wang, Y. Geng, M. Li, Q. Deng, Y. Tian, R. Chen, X. Zhu and Q. Liao, Carbon-Based Photothermal Superhydrophobic Materials with Hierarchical Structure Enhances the Anti-Icing and Photothermal Deicing Properties, *ACS Appl. Mater. Interfaces*, 2021, **13**(40), 48308–48321.

20 C. Zhao, S. Peng, B. Wu, L. Kang, L. Liang, M. Liu, L. Yang, W. Wang and X. Xu, Solar-driven superhydrophobic modified polyurethane sponge for rapid in-situ recovery of oil and microplastics in marine oil spill co-contamination, *J. Hazard. Mater.*, 2025, **500**, 140470.

21 H. Chu, Q. Xu, Z. Liu, N. Xu and H. Zhang, Eco-friendly photothermal superhydrophobic coatings: Recently advances in icephobic mechanisms, efficient photothermal conversion, and sustainable anti/de-icing technologies, *Adv. Colloid Interface Sci.*, 2025, **343**, 103565.

22 C. Chen, Z. Tian, X. Luo, G. Jiang, X. Hu, L. Wang, R. Peng, H. Zhang and M. Zhong, Cauliflower-like micro-nano structured superhydrophobic surfaces for durable anti-icing and photothermal de-icing, *Chem. Eng. J.*, 2022, **450**, 137936.

23 X. Qin, Q. Cong, J. Xu, T. Chen, J. Jin, C. Liu and M. Wang, Photothermal superhydrophobic coupled functional surface with active anti/de-icing performance, *Appl. Therm. Eng.*, 2025, **260**, 125031.

24 H. Gao, T. Yin, J. Ma, Y. Zhou, K. Li and J. Bao, Research Progress of Photothermal Superhydrophobic Surfaces for Anti-Icing/Deicing, *Molecules*, 2025, **30**(9), 1865.

25 W. Zhang, Y. Liu, F. Tao, Y. An, Y. Zhong, Z. Liu, Z. Hu, X. Zhang and X. Wang, An overview of biomass-based Oil/Water separation materials, *Sep. Purif. Technol.*, 2023, **316**, 123767.

26 Y. Zhang, X. Zhang, Y. Xu, Y. Li, X. Chen and Y. Zeng, Cellulose acetate-based composite fibrous membrane with asymmetric wettability for directional water transport and high-flux oil–water separation, *Cellulose*, 2024, **31**(4), 2493–2502.

27 X. Yu, X. Zhang, Y. Xing, H. Zhang, W. Jiang, K. Zhou and Y. Li, Development of Janus Cellulose Acetate Fiber (CA) Membranes for Highly Efficient Oil–Water Separation, *Materials*, 2021, **14**(20), 5916.

28 S. Subasini, A. Pius and P. Ananthi, Bioactive and Hydrolytically Degradable Cellulose Acetate/Polyurethane Wraps Enriched With Allium fistulosum Extract for Sustainable Food Packaging, *Asia-Pac. J. Chem. Eng.*, 2025, e70088.

29 Y. Zhang, Y. Wang, H. Zhang, Z. Wang and L. Li, Side-by-side PCL-PU fiber-based high-performance membranes for oil-water separation, *J. Environ. Chem. Eng.*, 2025, **13**(6), 120126.

30 Y. Zhang, T. Yu, W. Song, H. Zhang, Z. Wang and L. Li, Visible-light-induced self-cleaning polyurethane composite membrane with embedded amphiphilic nanoparticles for oil-water separation, *Sep. Purif. Technol.*, 2026, **382**, 136116.

31 Y. Wang, T. Jiang, J. Wu, S. Chen, M. Li, W. Wei, L. Zeng, J. Li and Z. Gao, Superhydrophobic-photothermal-insulating synergistic CNT/COF composite coatings for solar-powered crude oil restoration, *J. Hazard. Mater.*, 2025, **497**, 139690.

32 J. Shi, X. Wu, J. He, S. Mao, Y. Zhang, L. Shi and J. Tan, Synergistic interfacial reinforcement of hierarchically porous, self-standing, and hydrophobic biomass-derived composite membrane for oil/water separation, *Sep. Purif. Technol.*, 2026, **385**, 136379.

33 M. I. Jamil, S. Ayyaz, W. Ahmed, F. Haq, M. Yousaf, T. Iqbal, S. Mehmood and F. U. Khan, Sustainable carbon soot coatings for efficient oil-water separation and organic pollutants adsorption, *Colloids Surf., A*, 2026, **732**, 139139.

34 F. He, J. Li, Y. Wang, Z. Li, L. Wang, Y. Li, H. Chen, C. Wang, B. Liu, P. Ma, G. Dong and P. Zhou, Design of Cefotaxime Sodium-Loaded Polydopamine Coatings with Controlled Surface Roughness for Titanium Implants, *ACS Biomater. Sci. Eng.*, 2022, **8**(11), 4751–4763.

35 W. Chen, H. Ma and B. Xing, Electrospinning of multifunctional cellulose acetate membrane and its adsorption

properties for ionic dyes, *Int. J. Biol. Macromol.*, 2020, **158**, 1342–1351.
36 T. Riaz, A. Ahmad, S. Saleemi, M. Adrees, F. Jamshed, A. M. Hai and T. Jamil, Synthesis and characterization of polyurethane-cellulose acetate blend membrane for chromium (VI) removal, *Carbohydr. Polym.*, 2016, **153**, 582–591.
37 N. P. Shumbula, S. S. Nkabinde, Z. B. Ndala, S. Mpelane, M. P. Shumbula, P. S. Mdluli, Z. Njengele-Tetyana, P. Tetyana, T. Hlatshwayo, M. Mlambo and N. Moloto, Evaluating the antimicrobial activity and cytotoxicity of polydopamine capped silver and silver/polydopamine core-shell nanocomposites, *Arabian J. Chem.*, 2022, **15**(6), 103798.
38 X. Yang, Y. Zhou, Z. Sun, C. Yang and D. Tang, Polydopamine assists the continuous growth of zeolitic imidazolate framework-8 on electrospun polyacrylonitrile fibers as efficient adsorbents for the improved removal of Cr(VI), *New J. Chem.*, 2021, **45**(34), 15503–15513.
39 H. Chen, H. Zhang, Y. Zhang, W. Song, Z. Sun and L. Li, Nano-fishnet shaped PCL/PU-based composite membrane as superhydrophobic oil-water separator, *Sep. Purif. Technol.*, 2025, **359**, 130614.
40 H. Liu, W. Li, W. Wen, B. Luo, M. Liu, S. Ding and C. Zhou, Mechanical properties and osteogenic activity of poly(l-lactide) fibrous membrane synergistically enhanced by chitosan nanofibers and polydopamine layer, *Mater. Sci. Eng.*, 2017, **81**, 280–290.
41 A. Yao, Y. Yan, L. Tan, Y. Shi, M. Zhou, Y. Zhang, P. Zhu and S. Huang, Improvement of filtration and antifouling performance of cellulose acetate membrane reinforced by dopamine modified cellulose nanocrystals, *J. Membr. Sci.*, 2021, **637**, 119621.
42 W. Chong, R. Meng, Z. Liu, Q. Liu, J. Hu, B. Zhu, D. K. Macharia, Z. Chen and L. Zhang, Superhydrophilic Polydopamine-Modified Carbon-Fiber Membrane with Rapid Seawater-Transferring Ability for Constructing Efficient Hanging-Model Evaporator, *Adv. Fiber Mater.*, 2023, **5**(3), 1063–1075.
43 J. Lin, F. Lin, R. Liu, P. Li, S. Fang, W. Ye and S. Zhao, Scalable fabrication of robust superhydrophobic membranes by one-step spray-coating for gravitational water-in-oil emulsion separation, *Sep. Purif. Technol.*, 2020, **231**, 115898.
44 J. P. Youngblood and T. J. Mccarthy, Ultrahydrophobic polymer surfaces prepared by simultaneous ablation of polypropylene and sputtering of poly(tetrafluoroethylene) using radio frequency plasma, *Macromolecules*, 1999, **32**(20), 6800–6806.
45 X. Yang, Y. Liu, Y. Zhong and H. Chen, Ultra-durable photothermal anti-/de-icing superhydrophobic coating with water droplets freezing from the outside in[J], *J. Colloid Interface Sci.*, 2025, **682**, 1127–1139.
46 B. Yu, Z. Sun, Y. Liu, Y. Wu and F. Zhou, Photo-Thermal Superhydrophobic Sponge for Highly Efficient Anti-Icing and De-Icing, *Langmuir*, 2023, **39**(4), 1686–1693.
47 C. E. Tas, E. Berksun, D. Koken, S. Unal and H. Unal, Photothermal Waterborne Polydopamine/Polyurethanes with Light-to-Heat Conversion Properties, *ACS Appl. Polym. Mater.*, 2021, **3**(8), 3929–3940.
48 Y. Wang, M. Yu, Y. Qiu, X. Zhang and J. Han, Polydopamine-bridged Ag@diatomite composites for mechanically enhanced polymer interfaces and triple-synergistic antibacterial function, *Chem. Eng. J.*, 2025, **525**, 170729.
49 X. Li, X. Huang, S. Wang, Y. Qu, W. Yu, C. Ma, J. Ma, K. Zhang, X. Yue, H. Yue, J. Wang, M. Zhang and X. Deng, Insights into the Process and Mechanism of Polyethylenimine-Initiated Dopamine Polymerization for Precisely Regulating Their Dispersibility and Photothermal Properties, *Macromol*, 2025, **58**(21), 11756–11770.
50 S. Guzman-Sanchez, N. Patel and A. S. Rosado, Recent progress of polydopamine nanoparticles as advanced antimicrobial nanomaterials, *Front. Bioeng. Biotechnol.*, 2025, **13**, 1678136.
51 K. Zhang, J. Huang, S. Lu, Y. Hu, W. Pan and L. Liu, Multi-Scale Biomimetic Strategy: Robust Woven Wires with Photo-Thermal De-Icing and Spontaneous De-Wetting, *Adv. Funct. Mater.*, 2025, **35**(47), 2423043.
52 C.-H. Xue, H.-G. Li, X.-J. Guo, Y.-R. Ding, B.-Y. Liu, Q.-F. An and Y. Zhou, Superhydrophobic anti-icing coatings with self-deicing property using melanin nanoparticles from cuttlefish juice, *Chem. Eng. J.*, 2021, **424**, 130553.
53 H.-B. Yuan, M. Zhao, X. Lei, D. Sha, T. Xing and G. Chen, Fabrication of multifunctional cotton fabric with "pompon mum" shaped surface by ZIF-8 for applications in oil-water separation and anti-icing, *Prog. Org. Coat.*, 2024, **186**, 108056.
54 X. Wang, L. Tang, S. Fan and W. Fan, Novel Self-Healing Superhydrophobic Coating with Oil–Water Separation and Anti-Icing Properties, *Nanomaterials*, 2024, **14**(24), 1981.
55 H. Wang, P. Cao, S. Xu, G. Cui, Z. Chen and Q. Yin, Anti-icing performance of hydrophobic coatings on stainless steel surfaces, *Heliyon*, 2024, **10**(11), e32319.
56 N. Zhang, X. Kong, Y. Chang, W. Qiao, M. Zhang and R. Kang, Robust photothermal superhydrophobic concrete coating for efficient anti-icing/de-icing, *J. Building Eng.*, 2025, **101**, 111842.
57 L. Qiao, Z. Zhou, M. Wang and Z. He, Lignin Microsphere/TiO2 Composite-Based Melamine Sponge with Superhydrophobic and Photothermal Properties for Oil/Water Separation and Anti-Icing, *Langmuir*, 2025, **41**(21), 13233–13248.
58 X. Xiao, F. Yao, M. Huang, J. Wei and J. Wang, Electrothermal-Assisted Photothermal Lubrication Surfaces for Continuous Anti-Icing/Deicing in Multiple Low-Temperature Environments, *Langmuir*, 2024, **40**(32), 17151–17159.
59 T. Ma, J. Wei, W. Sun, S. Zhang, D. Wang, X. Yang, Z. Zhou, W. Tong and J. Wang, Durable Photothermal Superhydrophobic Coatings with Amorphous-Polymer Composite Structure Enhance Anti-Icing and Environment-Resistant Properties, *Langmuir*, 2025, **41**(43), 29051–29063.
60 M. Wang, L. Qiao, S. Ma and Z. He, Facile Preparation of Photothermal Superhydrophobic Melamine Sponge Decorated with MXene and Lignin Particles for Efficient Oil/Water Separation, Fast Crude Oil Recovery, and Active Deicing, *Langmuir*, 2024, **40**(11), 5978–5991.
61 L. Wang, J. Hu, X. Zhou, M. Liu, Y. Wu and H. Zheng, Modification-free bionic superhydrophobic laser-induced graphene (LIG) wearable strain sensor with superior anti-icing performance, *Chem. Eng. J.*, 2025, **508**, 161140.

62 S. Liu, Z. Zhu, Q. Zheng, K. Wang, F. Zhou, Q. Yang, X. Wang, L. Ye, Y. Chen, H. Liu and H. Li, Waxberry-liked micro-nanostructured, superhydrophobic surfaces with enhanced photothermal de-icing and passive anti-icing properties, *Chem. Eng. J.*, 2025, **503**, 158358.

63 T. Yang, Q. Lu, F. Ren, S. Xin, H. Zhang, H. Qiao, Z. Wang and L. Liu, A Fluorine-Free Superhydrophobic Micro–Nano Structured SiO2/TiN Coating for Anti-icing and Photothermal Deicing, *ACS Appl. Nano Mater.*, 2024, **7**(12), 14737–14747.